

Experimental demonstration of scalable quantum cryptographic conferencing

Haotao Zhu^{1,2,3}, Zhenhua Li⁴, Shuai Zhao⁵, Xiaodan Lyu⁶,
Shihao Ru^{1,3,7}, Yizhi Huang⁸, Zitong Xu^{1,3,9}, Rui Qu^{1,3,9},
Weibo Gao^{1,2,3,9,*}

¹School of Electrical & Electronic Engineering, Nanyang Technological University, Singapore, 639798, Singapore.

²Quantum Science and Engineering Centre (QSec), Nanyang Technological University, Singapore, Singapore.

³Division of Physics and Applied Physics, School of Physical and Mathematical Sciences, Nanyang Technological University, Singapore, 637371, Singapore.

⁴China Telecom Research Institute, Beijing, 102209, China.

⁵School of Cyberspace, Hangzhou Dianzi University, Hangzhou, 310018, China.

⁶Majulab, International Research Laboratory IRL 3654, CNRS, Université Côte d'Azur, Sorbonne Université, National University of Singapore, Nanyang Technological University, Singapore, Singapore.

⁷National Centre for Advanced Integrated Photonics, Nanyang Technological University, 21 Nanyang Link, Singapore, 637371, Singapore.

⁸China Telecom Quantum Information Technology Group Corporation Limited, Hefei, Anhui, 230088, China.

⁹Center for Quantum Technologies, Nanyang Technological University, Singapore, 637371, Singapore.

Abstract

Quantum network enables a variety of quantum information processing tasks, where multi-user quantum communication is one of the important objectives. Quantum cryptographic conferencing serves as an essential solution to establish secure keys to realize secure multi-user communications. However, existing QCC implementations have been fundamentally limited by the low probability of multi-user coincidence detection to measure or construct the Greenberger–Horne–Zeilinger (GHZ) entangled state. In this work, we report the experimental realization of QCC eliminating the need for coincidence detection, where the GHZ state is constructed by correlating detection events occurring within the coherence time, thereby greatly enhancing the success probability of GHZ-state measurement. Meanwhile, to establish and maintain high-visibility GHZ measurement among three independent users, we developed a three-party phase compensation scheme combined with precise temporal and polarization alignment within a time-bin–phase encoding framework. Furthermore, we designed an efficient pairing strategy to simplify subsequent data processing and enhance processing efficiency. Based on these techniques, we successfully performed QCC experiments over total channel losses of 66.3 dB, corresponding to 331.5 km of commercial fiber (0.2 dB/km), achieving secure key rates of 5.4 bit/s, whereas previous QCC experiments have been limited to 100 km. The results surpass the multi-user repeaterless bound in quantum networks, establishing a new regime of scalable, multi-user quantum communication and paving the way for metropolitan quantum networks.

1 Introduction

With rapid development of quantum technology, it is of central interest to establish secure and efficient quantum communication networks [1–3]. Quantum key distribution (QKD) [4–8] offers an effective method to establish information-theoretic security between two nodes by encoding information into quantum states of photons. It guarantees information-theoretic security based on the laws of quantum mechanics. However, in multi-user quantum networks, enabling secure communication among N parties with pairwise QKD requires the preparation of up to $N - 1$ copies of the key, which is highly inefficient [9]. An effective alternative is quantum cryptographic conferencing (QCC) [10–12], where secret keys are distilled directly from multi-party entangled states shared among multiple users.

Within this framework, various QCC protocols have been proposed [9, 13–22], which can be broadly categorized into two classes: entanglement-based and time-reversed approaches. In the entanglement-based scheme, a central node prepares a multi-party entangled state—such as a Greenberger–Horne–Zeilinger (GHZ) state [23]—and distributes it to multiple users, who then perform local measurements to establish a shared secret key. The time-reversed class refers to schemes in which the central node performs the measurement, and the GHZ state is effectively created through post-selection of the detection events [24]. Several experimental demonstrations following the time-reversed protocols have been reported [25, 26]. However,

both approaches are fundamentally limited by the intrinsically low probability of multi-photon coincidence detections, making them impractical for scalable scenarios.

In our experiment, we demonstrate three-user QCC experiment, achieving secure key generation over a total loss of 66.3 dB with a key rate of 5.4 bit/s, corresponding to 331.5 km of commercial fiber (0.2 dB/km), while previous QCC experiments have been limited to 100 km [18, 25, 26]. We constructed a three-user interference setup with active temporal and polarization feedback to ensure high-visibility interference between every two users. Furthermore, an efficient pairing strategy was designed to rapidly associate interference events, which accelerates valid-pair generation and simplifies the subsequent data processing. Based on this, we analyzed how the phase of each paired event affects the GHZ-state visibility, and accordingly developed a tailored phase-compensation method. As a result, we attain a GHZ-state measurement error of 39.42%, close to the 37.5% theoretical limit [14]. Our key rate performance surpasses the fundamental repeaterless bound for quantum networks, $R \leq -\log_2(1-\eta^2)$ [30, 31], for which the bound is 1.3×10^{-5} bit/s at our system frequency. Also, at a total channel loss of 51.8 dB, we achieve a key rate of 23.5 bit/s. From 51.8 to 66.3 dB, the key rate scaling remains approximately $O(\eta)$, surpassing the conventional key rate scaling of multi-party protocols [14, 15], where the key rate was limited by an $O(\eta^N)$ scaling in previous QCC experiments [25, 26].

2 Results

2.1 Protocol

A concise introduction to the mode-pairing QCC protocol is given here, with full details available in the Supplementary Information. In each round, Alice prepares the coherent state pulse $|\sqrt{k_A}e^{i\phi_A}\rangle$, where the intensity k_A is randomly chosen from the set $\{\mu, \nu, 0\}$, and the phase is randomly modulated from $\phi_A = \frac{2\pi}{16} \times n$. In this work, we set $0 < \nu < \mu < 1$ and $n = 0, 1, 2, \dots, 15$. Bob and Charlie similarly prepare coherent state pulses $|\sqrt{k_B}e^{i\phi_B}\rangle$ and $|\sqrt{k_C}e^{i\phi_C}\rangle$, respectively. Subsequently, the three coherent state pulses are sent to the GHZ analyzer, Eve. Eve splits each incoming pulse from every user into two parts using a beam splitter (BS), and then performs interference measurements between the adjacent users' pulses as shown in Fig. 1(a). Eve publicly announces the outcomes of each round of interference measurement. After N rounds, the users retain only those detection events in which one and only one detector registers a click. Following the pairing strategy detailed in the Supplementary Information, the basis choice and key value of each paired event are determined from the corresponding relative intensity and phase information. After performing basis sifting, key mapping, and data post-processing, the three-party mode-pairing QCC protocol produces the final shared secret key, and the length of the secure key can be expressed as [21]:

$$l \geq \underline{s}_{111}^Z \left[1 - H_2 \left(\bar{e}_{111}^{Z,ph} \right) \right] - f \bar{s}_{(\mu, \mu, \mu)}^Z \max \left[H_2 \left(\bar{E}_{A,B}^Z \right), H_2 \left(\bar{E}_{A,C}^Z \right) \right], \quad (1)$$

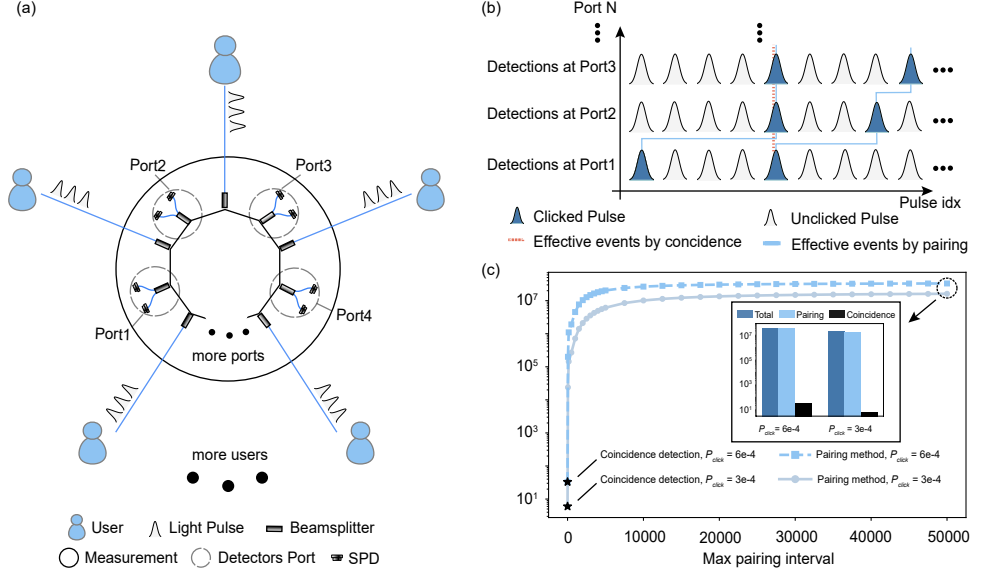


Fig. 1 (a) Multiple users send light pulses to a central measurement node, where a ring-structured detection architecture enables pairwise single-photon interference among all users through multiple detectors ports. (b) At each detection port, the pulse sequence indicates the responses details of single-photon detectors (SPD). Green pulses indicate time slots where at least one single-photon detector registers a click, whereas gray pulses correspond to no detector response. In the coincidence-based method, an effective event occurs only when all ports produce detections at the same pulse index. In contrast, the proposed pairing method identifies valid events by finding detector responses from each port within the coherence time window, without requiring detections to occur at identical pulse positions. (c) We present the experimental results showing the variation in the number of effective events as a function of the maximum pairing interval under two different pulse detection probabilities, P_{click} . For comparison, the number of effective events obtained from coincidence detection is also plotted, while Total denotes the total number of detected pulses. The Pairing results indicate that most detection clicks can be successfully paired, whereas the Coincidence events correspond to the expected P_{click}^2 fraction of the total detected clicks.

where $H_2(x) = -x \log_2 x - (1 - x) \log_2(1 - x)$ denotes the binary entropy function, f represents the error-correction efficiency. The single-photon contribution s_{111}^Z of the Z -basis paired events, as well as the associated phase error rate $e_{111}^{Z,\text{ph}}$, can be estimated through the decoy-state method [32, 33]. The number of paired events used for final key distillation, $s_{(\mu,\mu,\mu)}^Z$, as well as the marginal bit error rates $E_{A,B}^Z$ and $E_{A,C}^Z$ with Alice's key as the reference, can be directly obtained from the experimental data. Based on the Chernoff-Hoeffding method, \underline{x} and \bar{x} denote the lower and upper bounds of the observed value x , respectively.

2.2 Experiment

The experimental setting is shown in Fig. 2, a single laser is split into three beams for Alice, Bob, and Charlie, avoiding phase drift between independent lasers. The three-party phase issue is discussed in the Supplementary Information. Each party

modulates the continuous-wave light as follows: the light first passes through an intensity modulator to chop it into pulses with a repetition rate of 500 MHz. These pulses then pass through a Sagnac loop for decoy-state modulation, where the pulses are randomly prepared in one of four intensity states: reference, signal, decoy, or vacuum. The reference pulses are used for fiber-phase compensation. In the quantum-light zone, corresponding to the signal, decoy, and vacuum states, a phase modulator applies one of sixteen random phases, $\phi = \frac{2\pi}{16} \times n$ ($n = 0, 1, \dots, 15$), to realize phase randomization. In the reference zone, certain pulses are modulated with additional phases of $\pi/2$ or $3\pi/2$, as described in the Methods and Supplementary Information. The modulation signals are generated by three arbitrary waveform generators (two Tektronix AWG70002B and one Keysight M8195A), synchronized via a shared clock distribution module and operated in trigger mode to ensure precise timing alignment among all channels. Finally, the pulses are attenuated by an electrically variable optical attenuator to the single-photon level before being sent to the detection site. The detailed procedures for electrical signal synchronization and modulation, as well as optical modulation, will be described in the Supplementary Information. The experimental parameters used in our implementation are summarized in Table 1.

At the detection site, photons from Alice, Bob, and Charlie are split and interfere pairwise at three detection ports. Polarization feedback is applied to all six optical paths by monitoring the non-interfering PBS outputs with single-photon detectors and adjusting the EPC voltages to minimize their counts, thereby aligning the photon

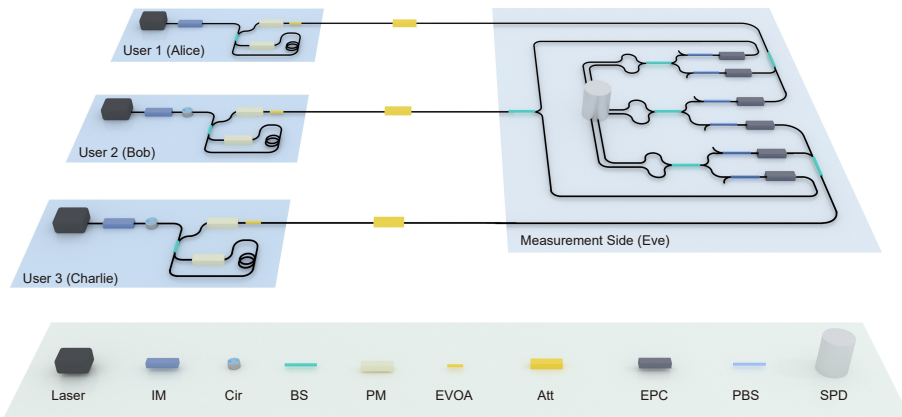


Fig. 2 Experimental Setup. A single laser is split into three beams serving as sources for Alice, Bob, and Charlie. Each beam is modulated by an intensity modulator and a Sagnac loop comprising a circulator, a beam splitter, and a phase modulator, followed by discrete 16-level phase modulation for randomization. The pulses are attenuated to the single-photon level using an electronically variable optical attenuator before transmission through either fiber or free-space attenuation channels. At the receiver, three BSs enable pairwise interferences between Alice–Bob, Bob–Charlie, and Charlie–Alice. Polarization feedback is applied using electronic polarization controllers and polarization beam splitters, and the outputs are detected by single-photon detectors. Abbreviations: IM, intensity modulator; Cir, circulator; BS, beam splitter; Att, attenuator; PM, phase modulator; EVOA, electronically variable optical attenuator; EPC, electronic polarization controller; SPD, single-photon detector.

Table 1 Experimental parameters and key results. The table summarizes the total loss, decoy-state settings, error-correction efficiency, detector performance, and the corresponding secure key rates for total losses of 51.8 dB and 66.3 dB.

Total loss (dB)	51.80	66.3
Channel attenuation loss (dB)	35.48	51.24
μ	0.2572	0.3535
ν	0.0209	0.0413
p_μ	0.15	0.15
p_ν	0.35	0.35
f	1.06	1.06
Measurement Side loss (dB)	2.51	2.51
Detector efficiency (%)	81	81
η	1.88×10^{-2}	6.18×10^{-3}
Key rate	1.64×10^{-7}	3.75×10^{-8}

polarizations. Temporal modes are aligned by statistically analyzing photon arrival times and tuning both the electronic delays of the arbitrary waveform generators and the optical delay lines, ensuring high-visibility interference (see Fig. 3(a-c)). The insertion loss of the optical delay lines (0.24 dB) is included in the total channel loss.

We collect the detection events from all six single-photon detectors and apply a sliding-window pairing algorithm that processes the data port-by-port (ports 1, 2, and 3) rather than in chronological order. The detailed implementation of this algorithm is described in the Methods and the Supplementary Information. The port-by-port strategy eliminates the need to account for which detector clicks first, simplifying the subsequent analysis, while the sliding-window algorithm improves the overall pairing efficiency. At both 51.8 dB and 66.3 dB total loss, the maximum pairing length was set to 100 μ s. With a 100 μ s acquisition window and a system clock rate of 500 MHz, most of the detection clicks can be paired for both total-loss conditions, given the corresponding channel transmittances η . The obtained pairs are assigned to the X - and Z - basis according to the protocol rules, where the Z -basis is used for secure key generation and the X -basis is employed for phase-error estimation and eavesdropping detection. Further implementation details are provided in the Supplementary Information.

Notably, reliable GHZ-state measurements require accurate estimation of the phase drift of the six optical paths. To this end, we use the reference pulses to estimate and compensate the fiber phase, and incorporate the extracted phases into parameter estimation, particularly for the X -basis error rate. Importantly, the signs of the three phase differences among the users (e.g., $\theta_B - \theta_A$, $\theta_C - \theta_B$, and $\theta_A - \theta_C$) must be pre-calibrated. We further present the GHZ-state error rates under different sign conventions, as shown in Fig. 3(d,e). The GHZ-state measurement error is minimized only when the phase of each user is correctly estimated, highlighting the collective phase dependence among the three parties. The procedure for determining the correct sign of these phase differences is described in detail in the Supplementary Information.

The experiments were carried out under total losses of 51.8 dB and 66.3 dB. At 51.8 dB, the Z - and X -basis error rates were 0.20% and 39.68%, respectively; at

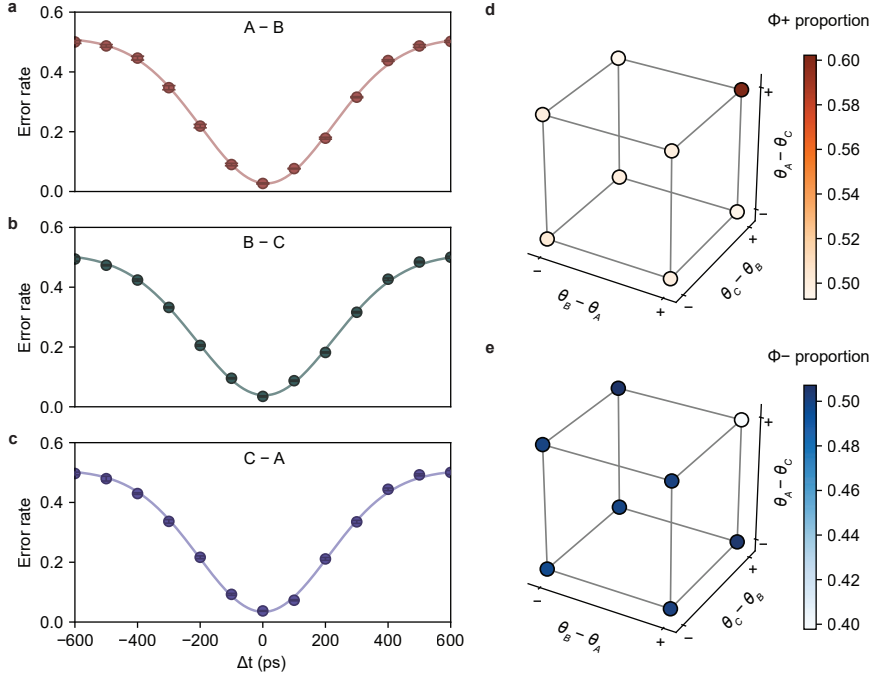


Fig. 3 Single-photon interference and collective phase dependence among users. (a–c) Error rate of single-photon interference as a function of the relative delay Δt between interfering pulses for each user pair: (a) Alice–Bob, (b) Bob–Charlie, and (c) Charlie–Alice. The error rate reaches a minimum at $\Delta t \approx 0$, indicating optimal temporal overlap and high-visibility interference. (d,e) Measured proportions of Φ^+ and Φ^- components as functions of the relative phase-difference signs $(\theta_B - \theta_A)$, $(\theta_C - \theta_B)$, and $(\theta_A - \theta_C)$. Each cube vertex represents one combination of sign conventions (“+” or “–”) corresponding to the measured proportion. “No flip” denotes the physically correct choice of phase-difference sign, while “flip” indicates an incorrect sign assignment. The results highlight the collective phase dependence among the three parties in GHZ-state measurement.

66.3 dB, they were 0.10% and 39.42%. The corresponding final key rates were 1.64×10^{-7} and 3.75×10^{-8} per pulse.

Given the quantum-light repetition rate of 143.52 MHz, the secure key generation rates are 23.5 bit/s and 5.39 bit/s at total losses of 51.8 dB and 66.3 dB, respectively. By converting the losses into channel transmittances of 6.6×10^{-6} and 2.3×10^{-7} , the transmittance ratio is about 28.2, whereas the measured key-rate ratio is 4.36. This near-linear yet slightly sub-linear dependence confirms the expected $O(\eta)$ scaling behavior [21] of the mode-pairing protocol and represents a significant improvement over the conventional multi-user scaling of $O(\eta^N)$ [14, 25, 26].

Given the quantum light repetition rate of 143.52 MHz, the secure key generation rates are 23.5 bit/s and 5.39 bit/s, respectively. Figure 4(a) shows that the key rate scales approximately linearly with the overall transmittance η , confirming the expected performance of the mode-pairing protocol. Notably, the obtained key rates surpass the repeaterless multi-end communication bound [34, 35], demonstrating the

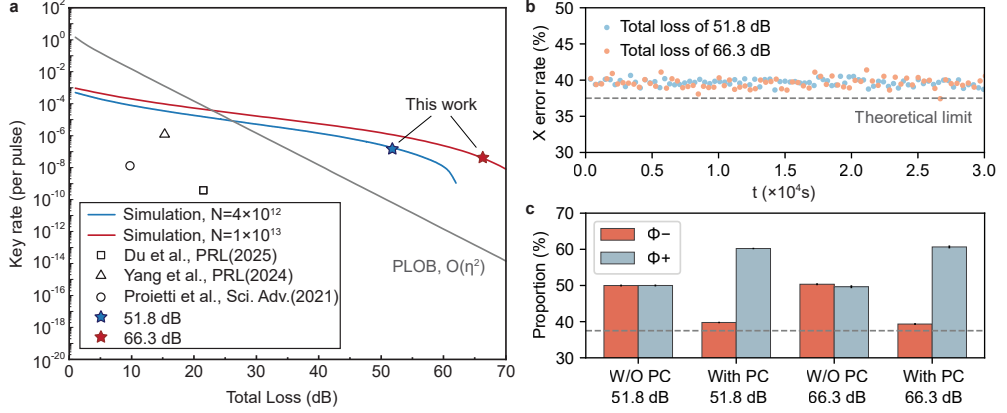


Fig. 4 Key-rate performance and phase-compensation results. **a.** Secret key rate versus total channel loss, compared with the repeaterless the repeaterless multi-end communication bound and previous experimental results [18, 25, 26]. **b.** Stability of the X -basis error rate over time, with the theoretical lower bound (37.5%) indicated. **c.** Error-rate distribution with and without phase compensation at 51.8 dB and 66.3 dB total loss, where W/O PC denotes the case without phase compensation and With PC denotes the case with phase compensation.

advantage of our implementation in efficiently utilizing single-photon interference even under high channel losses. In Fig. 4(b), the X -basis error rate fluctuates around the theoretical lower bound of 37.5% [14]. Owing to the presence of multi-photon components, this value represents the fundamental limit of the X -basis error. The long-term stability of the fluctuation further indicates that our system maintains stable phase coherence over extended operation periods. This is mainly due to our time-division-multiplexed phase compensation, the measured error approaches this bound. As shown in Fig. 4(c), the GHZ-state error rate strongly depends on the precision of phase compensation among all users. When the total phase is stabilized to 0 or π , the system deterministically projects onto $|\Phi^+\rangle$ or $|\Phi^-\rangle$, producing two distinct interference outcomes that correspond to complementary detector-response distributions. Any residual phase deviation blurs this distinction, reducing interference visibility and increasing X -basis error. Therefore, maximizing the phase contrast between these two GHZ-state projections is crucial for achieving high-fidelity multi-party interference and stable key generation.

3 Discussion and Conclusion

In conclusion, we have carried out QCC at the highest channel loss achieved by implementing simultaneous three-party phase, time, and polarization alignment to enable high interference visibility. By designing an effective pairing strategy and carefully analyzing the relation between the three-party phase and GHZ-state visibility, we minimized the GHZ-state measurement error. With these techniques, we successfully demonstrated the mode-pairing QCC experiment. Especially, at total channel losses of 51.8 dB and 66.3 dB, we obtained secret key rates of 1.64×10^{-7} and 3.75×10^{-8}

per pulse, corresponding to 23.5 and 5.4 bit/s. These results surpass the fundamental repeaterless bound [30, 31], and further confirm that the key-rate decay at two channel losses follows an approximately $O(\eta)$ scaling [21].

Our approach demonstrates the feasibility of long-distance, phase-stable, multi-user QCC based on single-photon interference and the efficient pairing strategy, without the need for entanglement distribution or quantum repeaters. The methods developed here—including multi-party phase compensation and optimized detection pairing—can be directly extended to larger-scale user networks and integrated photonic platforms. These results establish a practical benchmark for the future realization of scalable quantum communication networks.

Looking forward, in practical quantum networks, the distances from different users to the detection site are typically unequal, indicating that future studies could explore the performance of our scheme under asymmetric channel conditions. Furthermore, our experimental approach can be readily extended to include more users, substantially reducing resource consumption in multi-user quantum networks. Beyond multi-party quantum communication, efficient GHZ-state measurement can also benefit a wide range of quantum technologies, including multi-user network synchronization, quantum sensing, quantum network coherence, and measurement-based quantum computing.

4 Methods

Phase compensation for three parties

We employed time-division multiplexing to insert reference light, and the detailed emission timing diagram is provided in the Supplementary Information. For three-party QCC, it is necessary to perform three independent phase-difference estimations, with explicit derivations also given in the Supplementary Information. For any two users, the relative phase can be obtained from

$$\cos \theta = \frac{n_R - n_L}{n_R + n_L},$$

where n_R and n_L denote the detection counts of the right and left detectors, respectively. Since $\cos \theta$ alone does not uniquely determine θ within $[0, 2\pi)$, additional calibration is required. To resolve this ambiguity, we inserted auxiliary pulses with a $\pi/2$ phase or $3\pi/2$ phase offset in the reference-light region, ensuring that the phase between each user pair can be unambiguously identified as θ or $2\pi - \theta$. This procedure is essential for establishing the results of GHZ state measurement presented in Fig. 4 (c).

Three parties time alignment and polarization alignment

We aligned the polarization and timing of the six photon paths originating from the three detection ports to ensure indistinguishability among all interfering photons. Polarization feedback was implemented through the auxiliary output of each PBS, which provided real-time monitoring signals for automatic polarization correction. For timing feedback, two tunable optical delay lines were inserted in the

Bob–Charlie and Charlie–Alice channels and synchronized with the arbitrary waveform generators to achieve picosecond-level temporal alignment. This dual feedback scheme effectively compensated for slow drifts in fiber birefringence and path length variations, maintaining stable interference conditions throughout the experiment. As a result, high-visibility single-photon interference was achieved, as shown in Fig. 3, which constitutes the essential prerequisite for obtaining low-error GHZ-state measurement outcomes and confirming coherent three-party interference.

Pairing Strategy

As illustrated in the experimental setup (Fig. 2) of the main text, detection ports 1, 2, and 3 continuously generate photon detection events. Within a predefined maximum pairing length, these detection clicks must be grouped into valid pairs. Rather than pairing the events strictly in chronological order, we pair them sequentially according to the designated indices of the detection ports—for instance, port 1 corresponds to Alice–Bob, port 2 to Bob–Charlie, and port 3 to Charlie–Alice. This port-index–based pairing strategy simplifies subsequent data processing and significantly improves the overall pairing efficiency. To further satisfy the constraint imposed by the maximum pairing length, we implement a sliding-window algorithm in which the window size equals the predefined maximum length. This approach ensures that all valid pairs remain within the allowed temporal window while simultaneously reducing the computational complexity of the pairing process. The detailed procedure of the pairing algorithm and the pairing results are provided in the Supplemental Information.

Data availability. The data that support the findings of this study are available from the corresponding authors upon request.

Acknowledgements. This work was supported by A*STAR (M21K2c0116, M24M8b0004), the Singapore National Research Foundation (NRF-CRP22-2019-0004, NRF-CRP30-2023-0003, NRF-CRP31-0001, NRF2023-ITC004-001, and NRF-MSG-2023-0002), and the Singapore Ministry of Education Tier 2 Grant (MOE-T2EP50221-0005, MOE-T2EP50222-0018). We also acknowledge the support from the Zhejiang Provincial Natural Science Foundation of China Grant (No. LQ24A050005) and the Quantum Science and Technology - National Science and Technology Major Project (Grant No. 2024ZD0302200)

Author contributions. H.Z. and W.G. conceived the research. H.Z. designed and built the experimental setup. H.Z. carried out the experiment and performed data acquisition and post-processing. Z.L. and S.Z. performed theoretical modeling, protocol simulation, and secure key rate analysis. H.Z., Z.L. and W.G. co-wrote the manuscript with input from all authors. All authors discussed the results and revised the paper. W.G. supervised the project.

Competing interests. The authors declare no competing interests.

Additional information. Correspondence and requests for material should be addressed to wbgao@ntu.edu.sg.

References

- [1] Kimble, H.J.: The quantum internet. *Nature* **453**(7198), 1023–1030 (2008)
- [2] Wehner, S., Elkouss, D., Hanson, R.: Quantum internet: A vision for the road ahead. *Science* **362**(6412), 9288 (2018)
- [3] Pittaluga, M., Lo, Y.S., Brzozko, A., Woodward, R.I., Scalcon, D., Winnel, M.S., Roger, T., Dynes, J.F., Owen, K.A., Juárez, S., *et al.*: Long-distance coherent quantum communications in deployed telecom networks. *Nature* **640**(8060), 911–917 (2025)
- [4] Bennett, C.H., Brassard, G.: Quantum cryptography: Public key distribution and coin tossing. *Theoretical Computer Science* **560**, 7–11 (2014)
- [5] Ekert, A.K.: Quantum cryptography based on bell’s theorem. *Physical Review Letters* **67**(6), 661 (1991)
- [6] Gisin, N., Ribordy, G., Tittel, W., Zbinden, H.: Quantum cryptography. *Reviews of Modern Physics* **74**(1), 145 (2002)
- [7] Scarani, V., Bechmann-Pasquinucci, H., Cerf, N.J., Dušek, M., Lütkenhaus, N., Peev, M.: The security of practical quantum key distribution. *Reviews of Modern Physics* **81**(3), 1301–1350 (2009)
- [8] Xu, F., Ma, X., Zhang, Q., Lo, H.-K., Pan, J.-W.: Secure quantum key distribution with realistic devices. *Reviews of Modern Physics* **92**(2), 025002 (2020)
- [9] Epping, M., Kampermann, H., Bruß, D., *et al.*: Multi-partite entanglement can speed up quantum key distribution in networks. *New Journal of Physics* **19**(9), 093012 (2017)
- [10] Bose, S., Vedral, V., Knight, P.L.: Multiparticle generalization of entanglement swapping. *Physical Review A* **57**(2), 822 (1998)
- [11] Chen, K., Lo, H.-K.: Multi-partite quantum cryptographic protocols with noisy ghz states. *arXiv preprint quant-ph/0404133* (2004)
- [12] Murta, G., Grasselli, F., Kampermann, H., Bruß, D.: Quantum conference key agreement: A review. *Advanced Quantum Technologies* **3**(11), 2000025 (2020)
- [13] Grasselli, F., Kampermann, H., Bruß, D.: Finite-key effects in multipartite quantum key distribution protocols. *New Journal of Physics* **20**(11), 113014 (2018)
- [14] Fu, Y., Yin, H.-L., Chen, T.-Y., Chen, Z.-B.: Long-distance measurement-device-independent multiparty quantum communication. *Physical Review Letters* **114**(9), 090501 (2015)

- [15] Zhao, S., Zeng, P., Cao, W.-F., Xu, X.-Y., Zhen, Y.-Z., Ma, X., Li, L., Liu, N.-L., Chen, K.: Phase-matching quantum cryptographic conferencing. *Physical Review Applied* **14**(2), 024010 (2020)
- [16] Cao, X.-Y., Gu, J., Lu, Y.-S., Yin, H.-L., Chen, Z.-B.: Coherent one-way quantum conference key agreement based on twin field. *New Journal of Physics* **23**(4), 043002 (2021)
- [17] Carrara, G., Murta, G., Grasselli, F.: Overcoming fundamental bounds on quantum conference key agreement. *Physical Review Applied* **19**(6), 064017 (2023)
- [18] Proietti, M., Ho, J., Grasselli, F., Barrow, P., Malik, M., Fedrizzi, A.: Experimental quantum conference key agreement. *Science Advances* **7**(23), 0395 (2021)
- [19] Hahn, F., Jong, J., Pappa, A.: Anonymous quantum conference key agreement. *PRX Quantum* **1**(2), 020325 (2020)
- [20] Grasselli, F., Kampermann, H., Bruß, D.: Conference key agreement with single-photon interference. *New Journal of Physics* **21**(12), 123002 (2019)
- [21] Lu, Y.-S., Yin, H.-L., Xie, Y.-M., Fu, Y., Chen, Z.-B.: Repeater-like asynchronous measurement-device-independent quantum conference key agreement. *Reports on Progress in Physics* **88**(6), 067901 (2025)
- [22] Xie, Y.-M., Lu, Y.-S., Fu, Y., Yin, H.-L., Chen, Z.-B.: Multi-field quantum conferencing overcomes the network capacity limit. *Communications Physics* **7**(1), 410 (2024)
- [23] Greenberger, D.M., Horne, M.A., Zeilinger, A.: Going beyond bell's theorem, 69–72 (1989)
- [24] Pan, J.-W., Zeilinger, A.: Greenberger-horne-zeilinger-state analyzer. *Physical Review A* **57**(3), 2208 (1998)
- [25] Yang, K.-X., Mao, Y.-L., Chen, H., Dong, X., Zhu, J., Wu, J., Li, Z.-D.: Experimental measurement-device-independent quantum conference key agreement. *Physical Review Letters* **133**(21), 210803 (2024)
- [26] Du, Y., Liu, Y., Yang, C., Zheng, X., Zhu, S., Ma, X.-s.: Experimental measurement-device-independent quantum cryptographic conferencing. *Physical Review Letters* **134**(4), 040802 (2025)
- [27] Bell, J.S.: On the einstein podolsky rosen paradox. *Physics Physique Fizika* **1**(3), 195 (1964)
- [28] Zeng, P., Zhou, H., Wu, W., Ma, X.: Mode-pairing quantum key distribution.

Nature Communications **13**(1), 3903 (2022)

- [29] Xie, Y.-M., Lu, Y.-S., Weng, C.-X., Cao, X.-Y., Jia, Z.-Y., Bao, Y., Wang, Y., Fu, Y., Yin, H.-L., Chen, Z.-B.: Breaking the rate-loss bound of quantum key distribution with asynchronous two-photon interference. *PRX Quantum* **3**(2), 020315 (2022)
- [30] Pirandola, S., Laurenza, R., Ottaviani, C., Banchi, L.: Fundamental limits of repeaterless quantum communications. *Nature Communications* **8**(1), 15043 (2017)
- [31] Pirandola, S.: General upper bound for conferencing keys in arbitrary quantum networks. *IET Quantum Communication* **1**(1), 22–25 (2020)
- [32] Lo, H.-K., Ma, X., Chen, K.: Decoy state quantum key distribution. *Physical Review Letters* **94**(23), 230504 (2005)
- [33] Wang, X.-B.: Beating the photon-number-splitting attack in practical quantum cryptography. *Physical Review Letters* **94**(23), 230503 (2005)
- [34] Pirandola, S.: Bounds for multi-end communication over quantum networks. *Quantum Science and Technology* **4**(4), 045006 (2019)
- [35] Pirandola, S.: End-to-end capacities of a quantum communication network. *Communications Physics* **2**(1), 51 (2019)